Deep Earth rotational seismology

Rafael Abreu, Stephanie Durand, Sebastian Rost, Christine Thomas

Geophysical Journal International

Geophys. J. Int. (2023) **234,** 2366–2375
Advance Access publication 2023 June 19
GJI Seismology

https://doi.org/10.1093/gji/ggad245

Deep Earth rotational seismology

Rafael Abreu [1,2] Stephanie Durand,[3] Sebastian Rost [4] and Christine Thomas[2]

[1]*Institut de Physique du Globe de Paris, CNRS, Université de Paris, 75005 Paris, France. E-mail: rabreu@ipgp.fr*
[2]*Institut für Geophysik, Westfälische Wilhelms-Universität Münster, 48149 Münster, Germany*
[3]*Université Claude Bernard Lyon, UCBL, ENSL, UJM, CNRS, LGL-TPE, F-69622 Villeurbanne, France*
[4]*School of Earth and Environment, University of Leeds, Leeds LS2 9JT, UK*

Accepted 2023 June 11. Received 2023 June 3; in original form 2022 May 10

SUMMARY

Rotational seismology opens a new avenue to study the deep interior of the Earth. Using data from the Wettzell Observatorium, Germany, where a ring laser gyroscope and a 3-component translational broadband seismometer are co-located, we report the presence of clear S, ScS and SdS signals on both rotational and translational seismograms. Using S wave arrivals, we propose a new methodology to extract information on velocity changes in the Earth mantle and we show that, by combining both translational and rotational data, we are able to solve the well known velocity-depth ambiguity inherent to classical inverse problems. The methodology is validated using ray theory and 2.5-D finite-difference synthetics. We provide a proof-of-concept showing that future studies of the Earth's deep interior can be improved by combining translational and rotational records.

Key words: Theoretical seismology; Computational seismology: Wave propagation.

1 INTRODUCTION

Rotational seismology has been an emerging field in seismology in the past few years. It is based on the study of rotational motions generated by earthquakes, which have not been taken into account in seismology until recently because (i) they were considered to be small (Bouchon & Aki 1982) and (ii) because the rotational sensors were not sensitive enough to detect the small rotational motions related to distant earthquakes or controlled source experiments (Aki & Richards 2002). However, with the development of ring laser gyroscopes, originally designed to detect variations of the Earth's absolute rotation rate (e.g. Ezekiel & Balsamo 1977; Sanders *et al.* 1981; Chow *et al.* 1985), and more recently portable rotational seismometers, it has been shown that such instruments are able to record rotational ground motions generated by large earthquakes (McLeod *et al.* 1998; Pancha *et al.* 2000; Igel *et al.* 2021). From these pioneering works there is now a growing field of study reporting the observation of rotational motions generated by earthquakes and the benefits of studying rotational motions to better resolve Earth structure (Trifunac 2006; Fichtner & Igel 2009; Bernauer *et al.* 2009, 2012, 2014; Reinwald *et al.* 2016; Bernauer *et al.* 2020; Igel *et al.* 2021).

While rotational motions related to earthquakes recorded at ring-laser gyroscopes are by now well established, the development of portable instruments holds the potential for wider application of the developed methods (e.g. Bernauer *et al.* 2012, 2018 ; Brokešová *et al.* 2012; Jaroszewicz *et al.* 2012) and opens a broad spectrum of applications: (i) tilt corrections, to improve the quality of classic seismometer records (Lindner *et al.* 2017; Bernauer *et al.* 2020), (ii) better earthquake source characterization by combining rotational and translational data (e.g. Donner *et al.* 2016, 2018; Reinwald *et al.* 2016; Cao & Mavroeidis 2021; Yuan *et al.* 2021), (iii) application in seismic exploration where the combination of rotational and translational data enables carrying out array-type processing with single-station recordings such as wavefield separation, surface wave suppression and a direct isolation of the *S*-wave constituents (e.g. Li & van der Baan 2017; Sollberger *et al.* 2018), (iv) application in volcano seismology by helping to characterize the geometry of the associated source processes (e.g. Wassermann *et al.* 2020), (v) applications in structural engineering showing that rotational motions are important and their effect should be taken into account for future developments of earthquake-resistant design codes and microzonation planning (e.g. Trifunac 2006; Schreiber *et al.* 2009, 2021; Bońkowski *et al.* 2020; Zembaty *et al.* 2021; Murray-Bergquist *et al.* 2021; Guéguen & Astorga 2021) and more recently (vi) applications to the estimation of seismic anisotropy (Noe *et al.* 2022). Reviews on rotational seismology can be found in, for example Li & van der Baan (2017) and Schmelzbach *et al.* (2018).

One main technique of rotational seismology states that the ratio between the transverse acceleration a_T recorded by translational seismometers and the vertical rotation rate $\dot{\Omega}_z$ recorded by rotational seismometers is proportional to the phase velocity (Igel *et al.* 2005) as follows:

$$\frac{a_T}{\dot{\Omega}_z} = -2\beta_a = -2\frac{1}{p}, \tag{1}$$

where $\beta_a = \omega/k$ is the apparent shear wave velocity beneath the station with k the wave number and ω the angular frequency, and p [s km^{-1}] is the horizontal slowness or ray parameter (Igel *et al.*

2005; Fichtner & Igel 2009; Wassermann *et al.* 2016; Schmelzbach *et al.* 2018).

In this study, we propose to extend applications of the apparent shear wave velocity β_a to the study of the Earth's mantle. To do so, we first show that eq. (1) can be modified for imaging the Earth's lower mantle. We then validate this approach by using ray theory and 2.5-D finite-difference (FD) synthetics. We apply the method to recorded rotational and translational data from the Wettzell observatory and finally draw conclusions and propose future directions of this work.

2 IMAGING THE MANTLE COMBINING TRANSLATIONAL AND ROTATIONAL SEISMOGRAMS

To introduce a methodology for imaging the Earth's mantle by combining rotational and translational surface recordings, we rely on the definition of the apparent velocity given in eq. (1) and the ray parameter. When a wave is propagating in a layered medium, the application of Snell's law yields the definition of the ray parameter p which is constant along the ray and provides an estimate of the horizontal velocity as follows:

$$p = \frac{\sin i}{v} = s \sin i, \tag{2}$$

where i is the incidence angle, s is the slowness ($s = 1/v$) and v the velocity of the medium. The ray parameter p represents the apparent slowness of the wave front in the horizontal direction (horizontal slowness, Shearer 2019) and it can be related to the velocity of the medium v at, for instance, three different locations: the source, the receiver and the turning point (Stein & Wysession 2009)

$$p = \frac{\sin i_s}{v_s} = \frac{\sin i_0}{v_0} = \frac{\sin i_d}{v_d}, \tag{3}$$

where the subscripts (s, 0, d) refer to the source, receiver and turning (or deepest) point of the ray, respectively. If the wave does not reflect at an interface, then the deepest point of the ray will travel horizontally ($i_d = 90^\circ$), therefore the velocity of the medium at the deepest point of the ray is equal to the inverse of the slowness ($v = 1/p$).

Combining eqs (3) and (1), we obtain local values of the mantle velocity at the turning (deepest) point of the S travel path as follows:

$$v_d^S = \frac{1}{(p)^S} = -\frac{1}{2}\left(\frac{a_T}{\dot{\Omega}_z}\right)^S. \tag{4}$$

Eq. (4) can then be normalized with respect to PREM (Dziewonski & Anderson 1981) as follows:

$$\left(\frac{\delta v}{v}\right)^S = \frac{v_d^{S(\mathrm{obs})} - v_d^{S(\mathrm{PREM})}}{v_d^{S(\mathrm{PREM})}} = -\frac{1}{2}\left(\frac{a_T}{\dot{\Omega}_z}\right)^S (p)^S_{\mathrm{PREM}} - 1. \tag{5}$$

Note that eq. (5) can be written for any other 1-D earth model as well, for example STW105 (Kustowski *et al.* 2008), AK135 (Kennett *et al.* 1995), IASP91 (Kennett & Engdahl 1991) and that we can write eq. (5) as follows:

$$\left(\frac{\delta v}{v}\right)^S = \frac{(p)^S_{\mathrm{PREM}}}{(p)^S_{\mathrm{obs}}} - 1, \tag{6}$$

where $(p)_{\mathrm{obs}}$ stands for the observed horizontal slowness (or ray parameter). Eq. (6) is a generalization of eq. (5), where the value of the observed horizontal slowness can be found using rotational data and/or array techniques (Rost & Thomas 2002).

To access the information of rotational and translational data required by eq. (5), we need to compute the amplitude of the desired wave(s). Following Dahlen & Baig (2002), we define the synthetic and observed wave amplitudes, of the vertical rotation rate and/or transverse acceleration, to be the rms averages of the corresponding time-domain pulses $u_{\mathrm{syn}}(t)$ and $u_{\mathrm{obs}}(t)$ over the arrival interval $t_1 \leq t \leq t_2$ as follows:

$$A_{\mathrm{syn}} = \sqrt{\frac{1}{t_2 - t_1}\int_{t_1}^{t_2} u^2_{\mathrm{syn}}(t)dt}, \quad A_{\mathrm{obs}} = \sqrt{\frac{1}{t_2 - t_1}\int_{t_1}^{t_2} u^2_{\mathrm{obs}}(t)\mathrm{d}t}. \tag{7}$$

3 VALIDATION

To validate the presented methodology and to understand the information that can be obtained from the Earth's mantle, we perform several tests using ray theory followed by 2.5-D FD synthetics in 1-D/2-D earth models.

3.1 Ray theory

To test whether eq. (5) can help to resolve 1-D earth mantle heterogeneity, we perform synthetic tests and use TauP toolkit (Crotwell *et al.* 1999) implemented in Obspy (Krischer *et al.* 2015) for predicting delay times and ray parameters in 1-D models.

3.1.1 One layer models

We first test whether we can determine the shear velocity perturbation $(\delta v/v)^S$, with respect to certain 1-D earth model, and location of a layer of thickness (H) extending upward from the core–mantle boundary (CMB) in the rest of the paper referred as layer depth. To do so, we consider an event at 400 km depth recorded at 72° epicentral distance and a PREM 1-D background model including a layer of depth 691 km ($H = 2200$ km), and characterized by a $\delta v/v = -2.2$ per cent. We consider that this model is the true Earth that we aim to find. From it, using TauP, we compute the ray parameter for the S wave $(p)^S_{\mathrm{obs}}$ and traveltime $(t)^S_{\mathrm{obs}}$ that we expect to observe. We next use eq. (6) to predict which model can minimize the differential ray parameter $\delta p = (p)^S_{\mathrm{obs}} - (p)^S_{\mathrm{model}}$ and differential traveltime $\delta t = (t)^S_{\mathrm{obs}} - (t)^S_{\mathrm{model}}$. To do so, we linearly sample the model space with $\delta v/v \in [-6, 2]$ per cent and layer depth $\in [691, 0]$ km, with a total of $[200 \times 200]$ models. This allows us to deterministically compute the shear velocity perturbation $(\delta v/v)^S$ using eq. (6) and the differential traveltime δt data. Results are shown in Fig. 1, where the zero contour line obtained using eq. (6) refers to the models that agree with the observed data. Using eq. (6) alone we can resolve the velocity value of the 1-D anomaly but not the height of the layer (Fig. 1a), and the same happens for the differential traveltime δt (Fig. 1b). However, combining both solutions, the point where the two (zero contour) lines intersect, gives us the exact layer depth and velocity perturbation $\delta v/v$ (see Fig. 1c).

We next repeat the experiment for an event at 400 km depth recorded at 72° epicentral distance and with a 1-D background model including a layer of depth 291 km and characterized by a $\delta v/v = -4$ per cent (see Figs 1d–f). As before, we linearly sample the model space with $\delta v/v \in [-6, 2]$ per cent and depth $\in [691, 0]$ km, with a total of $[200 \times 200]$ models. Results show that, as in the previous case, using eq. (6) and differential traveltime δt information alone we can closely resolve the velocity value of the anomaly but not the depth of the layer (see Figs 1d and e). Combining both

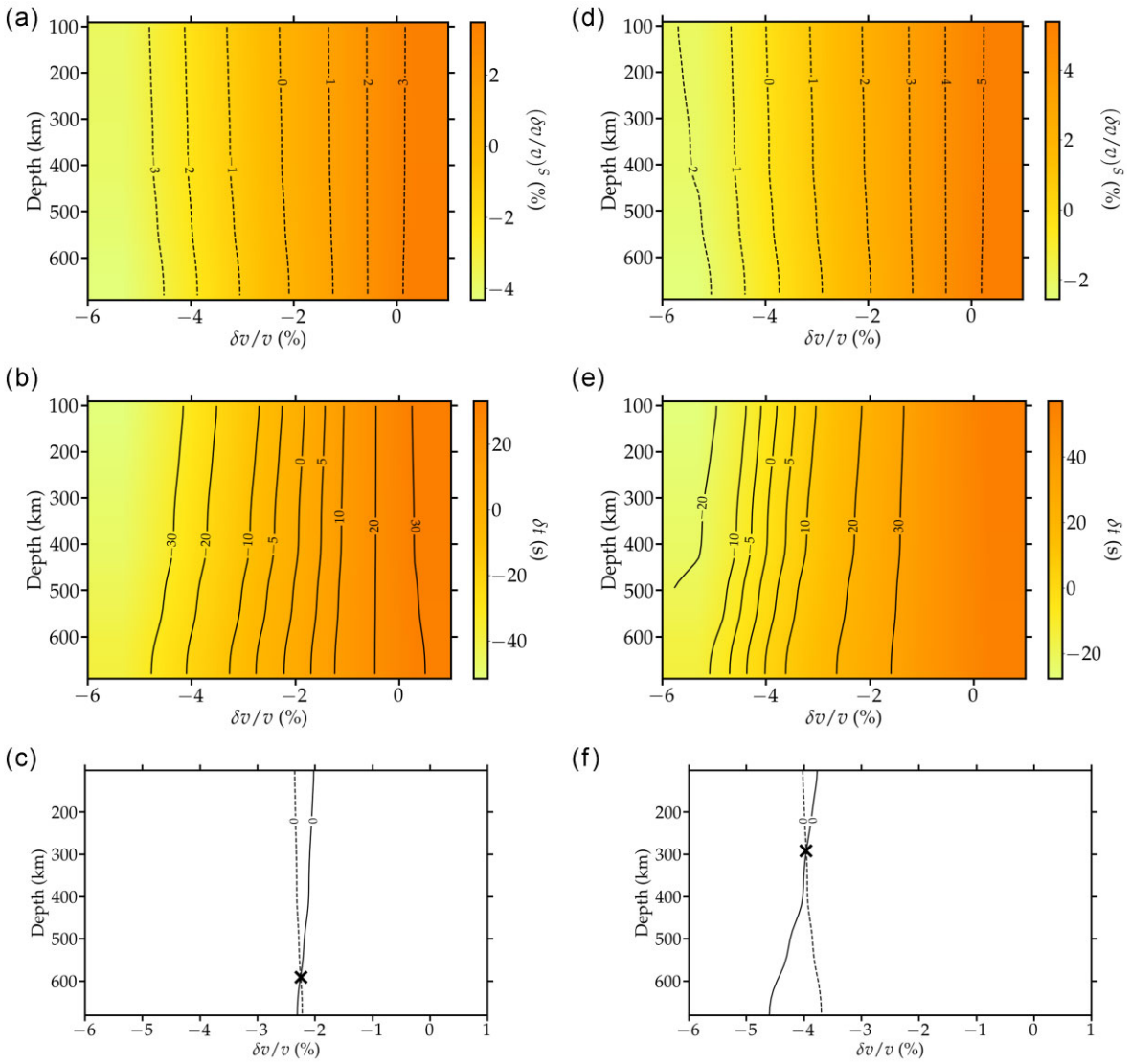

Figure 1. (a) Shear velocity perturbation $(\delta v/v)^S$ predicted using eq. (6) for an event at 70° epicentral distance and 400 km depth, with a low velocity depth of 591 km and $\delta v/v = -2.2$ per cent. (b) Differential traveltime δt predicted for the model presented in (a). (c) Intersection of zero contour lines in (a) and (b). Panels (d), (e) and (f) same as (a), (b) and (c) but for a model with depth of 291 km and $\delta v/v = -4$ per cent.

solutions we are again able to resolve both depth and $\delta v/v$ (see Fig. 1f). Without including any error information in the assumed observed data, we can resolve the well known velocity–depth ambiguity inherent to classical inverse problems (e.g. Bickel 1990; Lines 1993; Ross 1994) by combining translational and rotational data.

In order to understand the influence of errors on the measurements, we keep the last case (1-D anomaly perturbation with layer depth of 291 km and $\delta v/v = -4$ per cent) and now assume that only the ray parameter has been measured with a large uncertainty of ± 3 (s deg^{-1}). Repeating the previous experiments, predictions are shown in Figs 2(a) and (b). We can observe that traveltime and ray parameter contour curves do not intersect anymore preventing us to find a unique solution. In the same way, assuming errors of ± 3 (s) in traveltime measurements only, we observe that we are able to find a solution that matches observations although the height of the anomaly cannot be resoled well anymore (see Figs 2c and d). In practice however, such extreme errors of ± 3 (s deg^{-1}) in measurements of the ray parameter are not expected, while traveltime errors of ± 3 (s) are commonly accepted. Moreover, in practice we will most likely use various earthquake-station distances that will help reducing the effect of uncertainties. Therefore, we can conclude from these tests that uncertainties in ray parameter and/or traveltime measurements will affect inversion of the earth model, but combining accurate information of both measurements allows us to find more realistic 1-D models by solving the velocity–depth ambiguity.

3.1.2 *Influence of the reference model*

When aiming to find realistic models of the Earth, a single layer anomaly may turn out to be too simplistic in most cases. To evaluate the influence of 1-D models with 'n' unknown layers in eq. (5), we perform a grid search inversion using three models different from the model used to compute the observations (PREM): ak135f (Kennett & Engdahl 1991; Kennett *et al.* 1995), IASP91 (Kennett & Engdahl 1991; Kennet 1991) and SP6 (Morelli & Dziewonski 1993). To compute the results we assume an event at 72° epicentral distance and 400 km depth and with a PREM background model

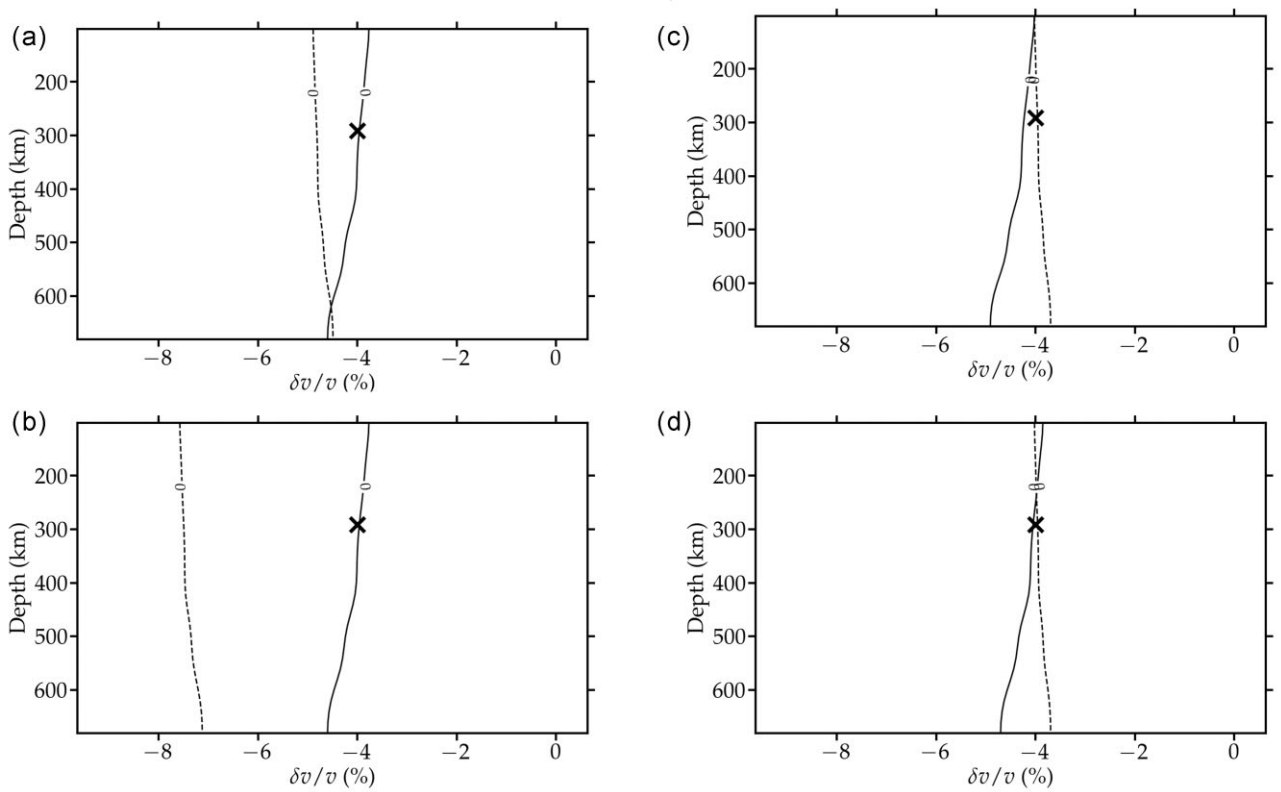

Figure 2. Zero contour lines of shear velocity perturbation $\delta v/v$ (dotted line) and differential traveltime δt (continuous line) for an event at 72° epicentral distance and 400 km depth with layer depth of 291 km and $\delta v/v = -4$ per cent with different assumed errors in the measurement of the ray parameter: (a) +0.1 (s deg^{-1}), b) +0.5 (s deg^{-1}) and traveltimes: (c) +1 (s) and (d) +3 (s).

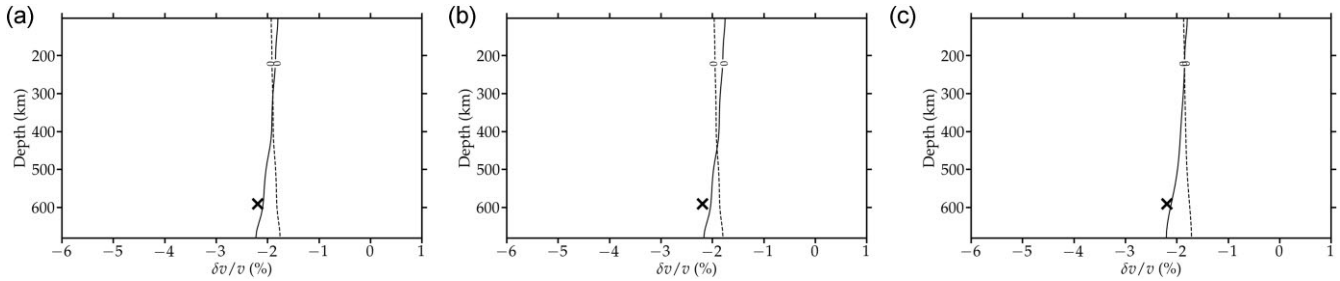

Figure 3. Predicted zero contour lines of shear velocity perturbation $\delta v/v$ (dotted line) and differential traveltime δt (continuous line) for an event at 72° epicentral distance and 400 km depth with layer depth of 591 km and $\delta v/v = -2.2$ per cent obtained as a grid search inversion assuming that observations are obtained using PREM and synthetic models are obtained using: (a) ak135f, (b) IASP91 and (c) SP6.

with an additional layer depth of 591 km with $\delta v/v = -2.2$ per cent. Using this model we compute the observed ray parameter for the S wave $(p)^S_{\rm obs}$ and traveltime $(t)^S_{\rm obs}$. As above, we linearly sample the model space with $\delta v/v \in [-6, 2]$ per cent and depth $\in$ [781, 0] km, with a total of [200 × 200] models for each one of the 1-D background models (ak135f, IASP91 and SP6).

Results of the grid search inversion are shown in Fig. 3, where we can observe that the three models predict a similar velocity perturbation of $\delta v/v \sim -1.89$ per cent but fail to predict the correct depth of the anomaly (591 km). All three models overestimate the elevation by ≥150 km. This is, however, expected since the synthetic data have been computed using PREM model. In practice, we never know which model should be chosen and this test shows that the height estimations might be overestimated. However, we are again only using one distance so in practice by combining several earthquake–station pairs the error on the height might be lowered. We conclude that the chosen background 1-D model may become relevant when finding the correct elevation of the anomaly, however, the combination of traveltime and ray parameter measurements improve results of the inversion.

3.2 2.5-D FD synthetics

To evaluate how effective the computation of the ray parameter is using eq. (1) for the S wave, we compute 21 s dominant period 2.5-D SH synthetics (Jahnke *et al.* 2008) for models with different shear velocity perturbations. Rotations are obtained directly from the simulations by taking the curl of the calculated velocity field. We first compute S ray parameter values for the 1-D model PREM for an event of 647.1 km, where we observe that results are nearly identical to those predicted by ray theory (see Fig. 4a). This allows us to benchmark the plane wave approximation given in eq. (1)

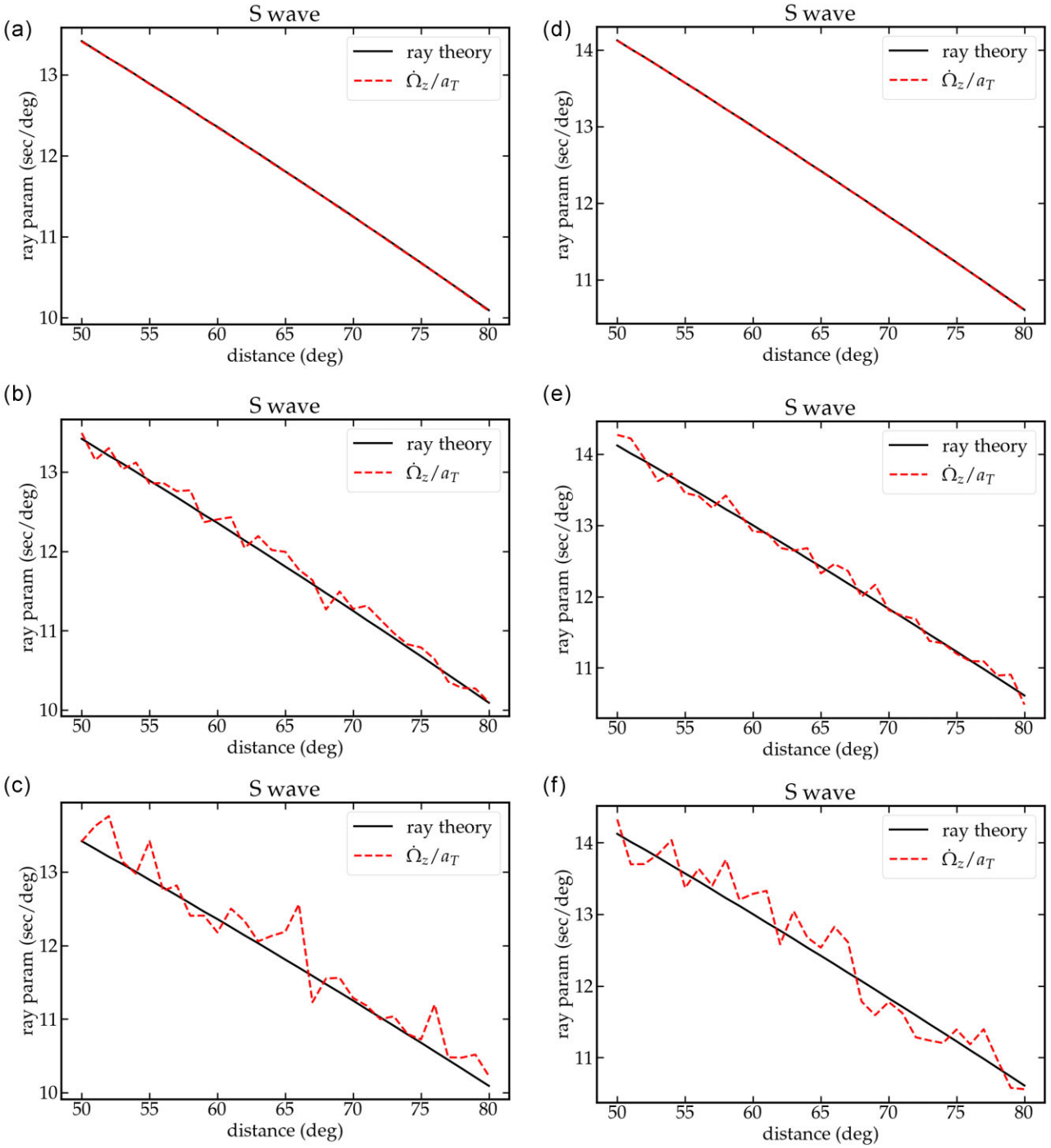

Figure 4. (a) Ray parameter predicted for PREM (black line) using eq. (1) and 2.5-D SH synthetics (red dashed line) with a dominant period of 21s for an event of 647.1 km depth. (b) Same as (a) but with added random noise of 5 per cent amplitude of the *S* wave. (c) Same as (a) but with added random noise of 10 per cent amplitude of the *S* wave. (d) Ray parameter predicted for PREM with a perturbation 1-D layer depth 591 km with $\delta v/v = -3$ per cent using eq. (1) and 2.5-D SH synthetics (red dashed line) with a dominant period of 21 s for an event of 400 km depth. (e) Same as (d) but with added random noise of 5 per cent amplitude of the *S* wave. (f) Same as (d) but with added random noise of 10 per cent amplitude of the *S* wave.

using numerical waveforms. We next assume an event of 400 km depth with 1-D background model PREM with a perturbation 1-D layer of depth 591 km with $\delta v/v = -3$ per cent. The obtained results are nearly identical to those predicted by ray theory up to a distance of $\sim 80^\circ$ (see Fig. 4d), which we explain to be due to the presence of other strong interference waves like, for example ScS. We also tested models with different velocity perturbations and/or layer depths and the general results remain the same for all cases. To measure the amplitude of the waves we apply eq. (7), the maximum of the envelope and the singular-value decomposition algorithm of the polarization analysis (Sollberger *et al.* 2018; Yuan *et al.* 2021) and results remain nearly identical.

To test the influence of noise on the signals, we add random Gaussian noise with zero mean and standard deviation of 0.1 with

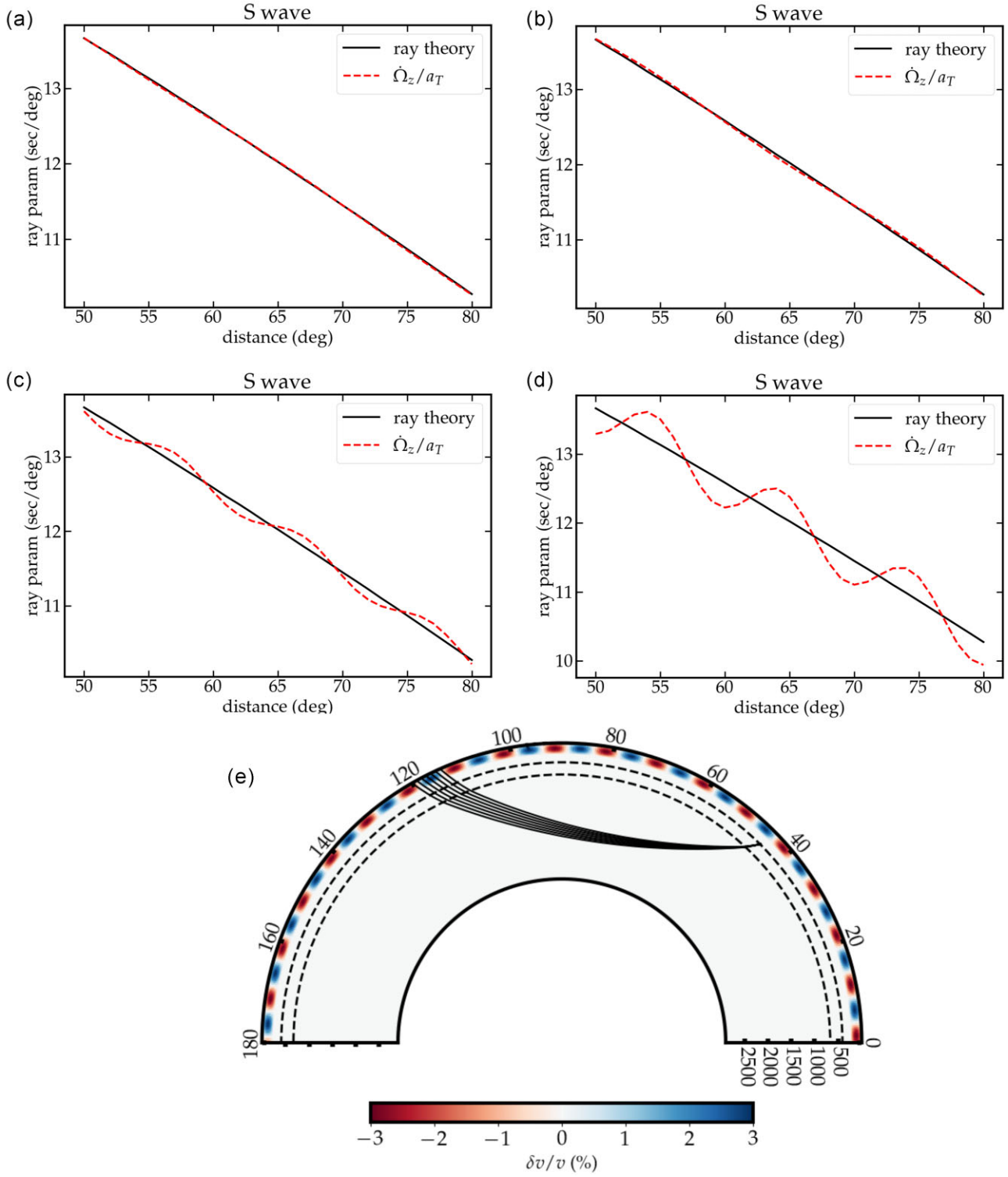

Figure 5. Ray parameter calculation results for 1-D earth model PREM with checkerboard shear velocity perturbations ($\delta v/v$) of ± 3 per cent with lateral dimensions of 5° and depths of (a) 20 km (b) 50 km (c) 110 km and (d) 300 km. (e) Checkerboard model used in (d).

5 and 10 per cent of the amplitude of the *S* wave. Results are, for the earth model PREM, shown in Figs 4(b) and (c), for the model with a layer depth 591 km characterized by $\delta v/v = -3$ per cent, in Figs 4(e) and (f). In all cases we can observe that measurements of the ray parameter, that contain more than 5 per cent noise, become unreliable.

We now test the influence of lateral heterogeneities in the ray parameter measurements. To do so, we implement four checkerboard models with perturbation ± 3 *per cent* ($\delta v/v$) with lateral dimension of 5° and different depths of 20, 50, 110 and 300 km (see Fig. 5e). Results are shown in Figs 5(a)–(d), where we can observe that large differences are observed for checkerboard models with

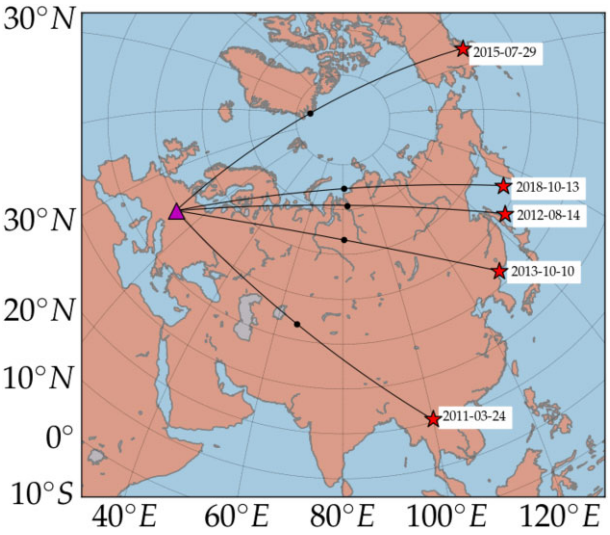

Figure 6. Events used in this study.

depth larger than 110 km. This is because our simulations have a dominant period of 21 s, which at the surface of the Earth, translates into a wavelengths of ∼60 km. We thus conclude that lateral heterogeneities, close to the surface of the Earth have a significant effects on the calculation of the ray parameter only at lengths larger than the dominant wavelength of the data. In real applications, there are strong velocity anomalies close to the surface due to the crust but the crust being on average 30 km thick it will generally be below the dominant wavelength of the *S* data. Moreover, tomographic models show heterogeneities that are at most ±2 per cent so again the test that we have performed is extreme. Finally, in practice we would use several earthquakes so that the ray parameter measurements should be improved. In the next section we apply the presented methodology to recorded data.

4 APPLICATION TO OBSERVED DATA

Due to the scarcity of deployed rotational seismometers around the world, we only apply the proposed methodology to data recorded at the Wettzell Observatory, Southern Germany, where both a ring laser gyroscope and a 3-component broadband seismometer are located. The proximity of both instruments allows us to make direct comparisons of the records. We collect events for the time period from 2010 to 2018, with magnitudes ranging from 6.0 to 7.9 M_w and a distance range from 70° to 76°. Choosing such a distance range allows us to sample deeper regions of the mantle and especially the D″ region. In total we analyse five events whose event details are listed in Table A1, with station location information listed in Table A2 in the Appendices (see Fig. 6). Data processing was performed using Obspy (Krischer *et al.* 2015) and included band-pass filtering between 3 and 25 s and a rotation to radial (*R*) and transverse components (*T*) for the translational records. We only kept records with a signal-to-noise ratio larger than 2.5.

Our first observation is a clear signal for the *S* wave in all events and in addition, a clear signal for the ScS wave as well as the SdS wave (e.g. Lay & Helmberger 1983; Weber 1993), the reflection off the D″ layer approximately 300 km above the CMB. These events show that it is indeed possible to detect deep Earth seismic arrivals with rotational instruments as well as determine their slowness values as shown in Fig. 7. This opens the possibility to detect D″ reflections in seismic data without the need to use a seismic array. Having so few measurements, prevent us to perform an inversion to find earth models that match the observations.

It is important to mention that while we can use eq. (5) to compute shear velocity perturbations of the Earth mantle, the use of eq. (4) helps to find local absolute velocity values which can be useful when studying absolute properties of the mantle and/or core. This is, however, different compared to the approach for tomographic inversions, that start from a known 1-D earth model that is subsequently modified to fit the observations.

5 DISCUSSION AND CONCLUSIONS

We have shown that teleseismic waves sampling the Earth's mantle can be clearly detected in rotational data. Using the combination of rotational and translational data, we have shown that we can successfully measure the ray parameter of the *S* wave, without using an array. Using the obtained ray parameter, we have presented a methodology to estimate 1-D earth velocity models that match both ray parameter and traveltime information. By matching both ray parameter and traveltime data, we are able to solve the velocity–depth ambiguity inherent to classical traveltime tomographic inversions (Bickel 1990; Lines 1993; Ross 1994).

The methodology presented in this work has the potential to provide means to refine, better constrain and perhaps to find consensus among different earth models and therefore help to decipher the nature of major structures such as the large low velocity provinces beneath the Pacific and Africa (Woodhouse & Dziewonski 1984) by providing sharper images of the Earth's mantle. It may also contribute to better image crustal thickness of large igneous provinces, which will help as a proxy for crustal composition and evolution (Korenaga *et al.* 2002; Korenaga 2011).

The possibility of determining the slowness of mantle seismic waves without the use of arrays provides strong potential to resolve Earth structure and to identify mantle sampling waves. A generalization of the approach to *P* waves to obtain better estimates of mantle velocity anomalies is possible and will be pursued in future.

In addition, we have detected the presence of ScS and SdS waves in two events (see Fig. 7) and the calculation of traveltime and ray parameters of these waves seem in agreement with observations. We found however, the limitation of computing ray parameters using amplitude informations because these two waves are subjected to

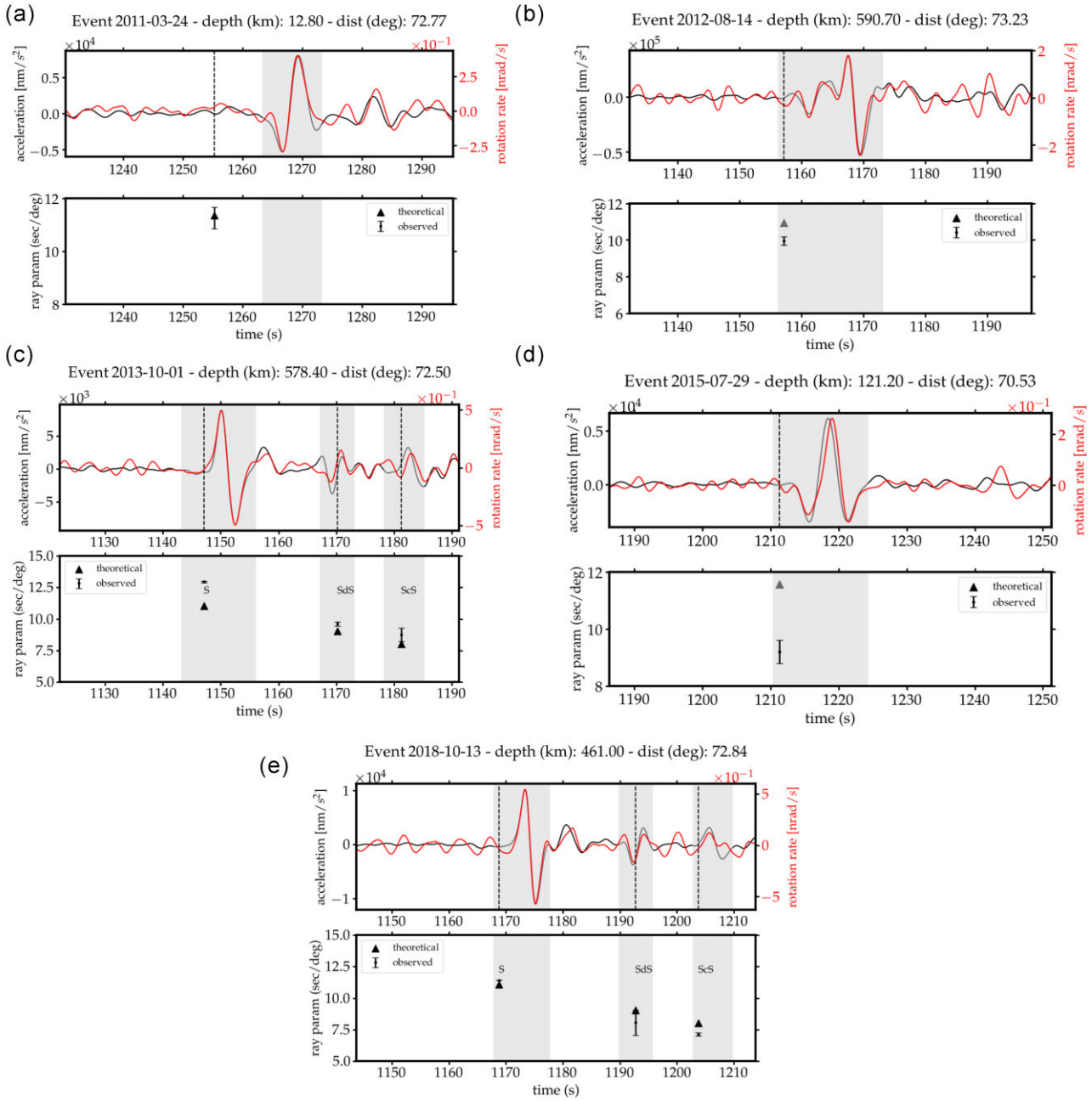

Figure 7. (b) Transverse acceleration (black curve) and vertical rotation rate (red curve) used for measuring the *S*-wave ray parameter and differential traveltime (PREM theoretical traveltime in dotted vertical line) of the events of (a) 2011-03-24 (Myanmar), (b) 2012-08-14 and (c) 2013-10-01 (both at th Sea of Okhotsk), (d) 2015-07-29 (Southern Alaska) and (e) 2018-10-13 (northwest of Kuril Islands). Theoretical SdS slownesses were obtained from the PWDK Earth model (Weber & Davis 1990) which places the D″ layer at 2605 km depth.

the influence of crustal reverberation and/or precursors and/or other waves that pollute their amplitudes thus interfering with the accurate ray parameter calculation. Presently, studying small-scale structures of the lower mantle, such as D″ and ULVZs, with rotational data is also a challenge due to the sparsity of permanent rotational sensor deployments and low sensitivity. Technological improvement of new portable rotational seismometers as well as their global installation can potentially provide the advantage of array measurements to larger parts of the globe. Here we provide a method that might make use of the potentially improved station coverage with rotational sensors in the future.

ACKNOWLEDGMENTS

The authors acknowledge constructive comments from Heiner Igel and one anonymous reviewer that helped to improve the quality and clarity of the work. RA was supported by the DFG project EARLY AB887/1-1. SR has been partially supported by NERC

grant NE/R012199/1 and support of a research visit by DAAD-France grant 9171428 and a WWU Fellow scholarship through the WWU Internationalisierungsfonds grant.

DATA AVAILABILITY

Data used in this work are available and have been downloaded with Obspy (Krischer *et al.* 2015) from the German Regional Seismic Network (GR, doi: https://doi.org/10.25928/mbx6-hr74), GRSN Station Wettzell (WET) and the geophysics web-page of the Ludwig Maximilian University of Munich (https://erde.geophysik.uni-muenchen.de/), network BayernNetz (BW, doi: https://doi.org/10.7914/SN/BW) and Wettzell ring laser (RLAS) located at the Wettzell Geodetic Observatory.

REFERENCES

Aki, K. & Richards, P.G., 2002. *Quantitative Seismology,* 2nd edn, Univ. Science Books.

Bernauer, F. *et al.*, 2018. BlueSeis3A: full characterization of a 3C broadband rotational seismometer, *Seismol. Res. Lett.,* **89**(2A), 620–629.

Bernauer, F., Wassermann, J. & Igel, H., 2020. Dynamic tilt correction using direct rotational motion measurements, *Seismol. Soc. Am.,* **91**(5), 2872–2880.

Bernauer, M., Fichtner, A. & Igel, H., 2009. Inferring earth structure from combined measurements of rotational and translational ground motions, *Geophysics,* **74**(6), WCD41–WCD47.

Bernauer, M., Fichtner, A. & Igel, H., 2012. Measurements of translation, rotation and strain: new approaches to seismic processing and inversion, *J. Seismol.,* **16**(4), 669–681.

Bernauer, M., Fichtner, A. & Igel, H., 2014. Reducing nonuniqueness in finite source inversion using rotational ground motions, *J. geophys. Res.,* **119**(6), 4860–4875.

Bickel, S.H., 1990. Velocity-depth ambiguity of reflection traveltimes, *Geophysics,* **55**(3), 266–276.

Bońkowski, P.A., Bobra, P., Zembaty, Z. & Jędraszak, B., 2020. Application of rotation rate sensors in modal and vibration analyses of reinforced concrete beams, *Sensors,* **20**(17), doi:10.3390/s20174711.

Bouchon, M. & Aki, K., 1982. Strain, tilt, and rotation associated with strong ground motion in the vicinity of earthquake faults, *Bull. seism. Soc. Am.,* **72**(5), 1717–1738.

Brokešová, J., Málek, J. & Kolínskỳ, P., 2012. Rotaphone, a mechanical seismic sensor system for field rotation rate measurements and its in situ Calibration, *J. Seismol.,* **16**(4), 603–621.

Cao, Y. & Mavroeidis, G.P., 2021. Simulation of near-fault ground strains and rotations from actual strike-slip earthquakes: case studies of the 2004 M w 6.0 Parkfield, the 1979 Mw 6.5 Imperial Valley and the 1999 Mw 7.5 Izmit earthquakes, *Geophys. J. Int.,* **226**(3), 1920–1947.

Chow, W., Gea-Banacloche, J., Pedrotti, L., Sanders, V., Schleich, W. & Scully, M., 1985. The ring laser gyro, *Rev. Modern Phys.,* **57**(1), 61.

Crotwell, H.P., Owens, T.J. & Ritsema, J., 1999. The TauP Toolkit: flexible seismic travel-time and ray-path utilities, *Seismol. Res. Lett.,* **70**(2), 154–160.

Dahlen, F. & Baig, A.M., 2002. Fréchet kernels for body-wave amplitudes, *Geophys. J. Int.,* **150**(2), 440–466.

Donner, S., Bernauer, M. & Igel, H., 2016. Inversion for seismic moment tensors combining translational and rotational ground motions, *Geophys. J. Int.,* **207**(1), 562–570.

Donner, S., Igel, H., Hadziioannou, C. *et al.*, 2018. Retrieval of the seismic moment tensor from joint measurements of translational and rotational ground motions: sparse networks and single stations, in *Moment Tensor Solutions,* pp. 263–280, Springer.

Dziewonski, A.M. & Anderson, D.L., 1981. Preliminary reference Earth model, *Phys. Earth planet. Inter.,* **25**(4), 297–356.

Ezekiel, S. & Balsamo, S., 1977. Passive ring resonator laser gyroscope, *Appl. Phys. Lett.,* **30**(9), 478–480.

Fichtner, A. & Igel, H., 2009. Sensitivity densities for rotational ground-motion measurements, *Bull. seism. Soc. Am.,* **99**(2B), 1302–1314.

Guéguen, P. & Astorga, A., 2021. The torsional response of civil engineering structures during earthquake from an observational point of view, *Sensors,* **21**(2), doi:10.3390/s21020342.

Igel, H., Schreiber, U., Flaws, A., Schuberth, B., Velikoseltsev, A. & Cochard, A., 2005. Rotational motions induced by the M8.1 Tokachi-oki earthquake, September 25, 2003, *Geophys. Res. Lett.,* **32**(8), doi:10.1029/2004GL022336.

Igel, H. *et al.*, 2021. Romy: a multi-component ring laser for geodesy and geophysics, *Geophys. J. Int.,* **225**(1), 684–698.

Jahnke, G., Thorne, M.S., Cochard, A. & Igel, H., 2008. Global SH-wave propagation using a parallel axisymmetric spherical finite-difference scheme: application to whole mantle scattering, *Geophys. J. Int.,* **173**(3), 815–826.

Jaroszewicz, L.R., Krajewski, Z. & Teisseyre, K.P., 2012. Usefulness of AFORS—autonomous fibre-optic rotational seismograph for investigation of rotational phenomena, *J. Seismol.,* **16**(4), 573–586.

Kennet, B., 1991. IASPEI 1991 seismological tables, *Terra Nova,* **3**(2), 122–122.

Kennett, B. & Engdahl, E., 1991. Traveltimes for global earthquake location and phase identification, *Geophys. J. Int.,* **105**(2), 429–465.

Kennett, B.L., Engdahl, E. & Buland, R., 1995. Constraints on seismic velocities in the Earth from traveltimes, *Geophys. J. Int.,* **122**(1), 108–124.

Korenaga, J., 2011. Velocity–depth ambiguity and the seismic structure of large igneous provinces: a case study from the Ontong Java Plateau, *Geophys. J. Int.,* **185**(2), 1022–1036.

Korenaga, J., Kelemen, P.B. & Holbrook, W.S., 2002. Methods for resolving the origin of large igneous provinces from crustal seismology, *J. geophys. Res.,* **107**(B9), ECV 1–1-ECV 1-27.

Krischer, L., Megies, T., Barsch, R., Beyreuther, M., Lecocq, T., Caudron, C. & Wassermann, J., 2015. ObsPy: a bridge for seismology into the scientific Python ecosystem, *Comput. Sci. Discov.,* **8**(1), doi:10.1088/1749-4699/8/1/014003.

Kustowski, B., Ekström, G. & Dziewoński, A., 2008. Anisotropic shear-wave velocity structure of the Earth's mantle: a global model, *J. geophys. Res.,* **113**(B6), doi:10.1029/2007JB005169.

Lay, T. & Helmberger, D.V., 1983. A lower mantle S-wave triplication and the shear velocity structure of D″, *Geophys. J. Int.,* **75**(3), 799–837.

Li, Z. & van der Baan, M., 2017. Tutorial on rotational seismology and its applications in exploration geophysics, *Geophysics,* **82**(5), W17–W30.

Lindner, F., Wassermann, J., Schmidt-Aursch, M.C., Schreiber, K.U. & Igel, H., 2017. Seafloor ground rotation observations: potential for improving signal-to-noise ratio on horizontal OBS components, *Seismol. Res. Lett.,* **88**(1), 32–38.

Lines, L., 1993. Ambiguity in analysis of velocity and depth, *Geophysics,* **58**(4), 596–597.

McLeod, D., Stedman, G., Webb, T. & Schreiber, U., 1998. Comparison of standard and ring laser rotational seismograms, *Bull. seism. Soc. Am.,* **88**(6), 1495–1503.

Morelli, A. & Dziewonski, A.M., 1993. Body wave traveltimes and a spherically symmetric P-and S-wave velocity model, *Geophys. J. Int.,* **112**(2), 178–194.

Murray-Bergquist, L., Bernauer, F. & Igel, H., 2021. Characterization of six-degree-of-freedom sensors for building health monitoring, *Sensors,* **21**(11), doi:10.3390/s21113732.

Noe, S., Yuan, S., Montagner, J.-P. & Igel, H., 2022. Anisotropic elastic parameter estimation from multicomponent ground-motion observations: a theoretical study, *Geophys. J. Int.,* **229**(2), 1462–1473.

Pancha, A., Webb, T., Stedman, G., McLeod, D. & Schreiber, K., 2000. Ring laser detection of rotations from teleseismic waves, *Geophys. Res. Lett.,* **27**(21), 3553–3556.

Reinwald, M., Bernauer, M., Igel, H. & Donner, S., 2016. Improved finite-source inversion through joint measurements of rotational and translational ground motions: a numerical study, *Solid Earth,* **7**(5), 1467–1477.

Ross, W.S., 1994. The velocity-depth ambiguity in seismic traveltime data, *Geophysics,* **59**(5), 830–843.

Rost, S. & Thomas, C., 2002. Array seismology: methods and applications, *Rev. Geophys.,* **40**(3), 2–1.

Sanders, G., Prentiss, M. & Ezekiel, S., 1981. Passive ring resonator method for sensitive inertial rotation measurements in geophysics and relativity, *Optics Lett.,* **6**(11), 569–571.

Schmelzbach, C. *et al.*, 2018. Advances in 6C seismology: applications of combined translational and rotational motion measurements in global and exploration seismology, *Geophysics,* **83**(3), WC53–WC69.

Schreiber, K., Velikoseltsev, A., Carr, A. & Franco-Anaya, R., 2009. The application of fiber optic gyroscopes for the measurement of rotations in structural engineering, *Bull. seism. Soc. Am.,* **99**(2B), 1207–1214.

Shearer, P.M., 2019. *Introduction to Seismology,* Cambridge Univ. Press.

Simonelli, A., Desiderio, M., Govoni, A., De Luca, G. & Di Virgilio, A., 2021. Monitoring local earthquakes in central Italy using 4C single station data, *Sensors,* **21**(13), doi:10.3390/s21134297.

Sollberger, D., Greenhalgh, S.A., Schmelzbach, C., Van Renterghem, C. & Robertsson, J.O., 2018. 6-C polarization analysis using point measurements of translational and rotational ground-motion: theory and applications, *Geophys. J. Int.,* **213**(1), 77–97.

Stein, S. & Wysession, M., 2009. *An Introduction to Seismology, Earthquakes, and Earth Structure,* John Wiley & Sons.

Trifunac, M.D., 2006. Effects of torsional and rocking excitations on the response of structures, in *Earthquake Source Asymmetry, Structural Media and Rotation Effects,* pp. 569–582, Springer.

Wassermann, J., Wietek, A., Hadziioannou, C. & Igel, H., 2016. Toward a single-station approach for microzonation: using vertical rotation rate to estimate Love-wave dispersion curves and direction finding, *Bull. seism. Soc. Am.,* **106**(3), 1316–1330.

Wassermann, J., Bernauer, F., Shiro, B., Johanson, I., Guattari, F. & Igel, H., 2020. Six-axis ground motion measurements of caldera collapse at Kīlauea volcano, Hawai'i—more data, more puzzles?, *Geophys. Res. Lett.,* **47**(5), doi:10.1029/2019GL085999.

Weber, M., 1993. P-and S-wave reflections from anomalies in the lowermost mantle, *Geophys. J. Int.,* **115**(1), 183–210.

Weber, M. & Davis, J., 1990. Evidence of a laterally variable lower mantle structure from P-and S-waves, *Geophys. J. Int.,* **102**(1), 231–255.

Woodhouse, J.H. & Dziewonski, A.M., 1984. Mapping the upper mantle: three-dimensional modeling of earth structure by inversion of seismic waveforms, *J. geophys. Res.,* **89**(B7), 5953–5986.

Yuan, S., Gessele, K., Gabriel, A.-A., May, D.A., Wassermann, J. & Igel, H., 2021. Seismic source tracking with six degree-of-freedom ground motion observations, *J. geophys. Res.,* **126**(3) , doi:10.1029/2020JB021112.

Zembaty, Z., Bernauer, F., Igel, H. & Schreiber, K.U., 2021. Rotation rate sensors and their applications, *Sensors,* **21**(16), doi:10.3390/s21165344.

APPENDIX: DATA

Table A1. Earthquakes used in this study.

Date	Time	Latitude (°)	Longitude (°)	Depth (km)	M_w	Source region
2011-03-24	2011-03-24T13:55:13.390000Z	20.6298	99.9178	12.8	6.8	Myanmar
2012-08-14	2012-08-14T02:59:38.860000Z	49.75	145.3057	590.7	7.7	Sea of Okhotsk
2013-10-01	2013-10-01T03:38:21.390000Z	53.1368	152.8959	578.4	6.7	Sea of Okhotsk
2015-07-29	2015-07-29T02:35:58.120000Z	59.9722	−153.3246	121.2	6.4	Southern Alaska
2018-10-13	2018-10-13T11:10:22.400000Z	52.8549	153.2429	461.0	6.7	Northwest of Kuril Islands

Table A2. Stations used in this study.

Station	Network	DOI
Wettzell ring laser (RLAS)	BayernNetz (BW)	https://doi.org/10.7914/SN/BW
GRSN Station Wettzell (WET)	German Regional Seismic Network (GR)	https://doi.org/10.25928/mbx6-hr74